Nanoscale

PAPER

View Article Online
View Journal | View Issue

Cite this: *Nanoscale*, 2023, **15**, 1925

Indocyanine green derived carbon dots with significantly enhanced properties for efficient photothermal therapy†

Yuxiang Jiang,‡[a] Zhuomin Tan,‡[b] Tianshu Zhao,‡[a] Jiajia Wu,[a] Ya Li,[b] Yinnong Jia*[b] and Zhili Peng*[a]

Received 30th October 2022,
Accepted 19th December 2022

DOI: 10.1039/d2nr06058b

rsc.li/nanoscale

A simple yet effective strategy to enhance the properties of traditional dye indocyanine green (ICG) in all aspects was proposed and demonstrated. Specifically, indocyanine green-derived carbon dots (ICGCDs) were synthesized from ICG *via* a simple hydrothermal treatment. The ICGCDs exhibited significantly enhanced thermal stability and anti-photobleaching compared to ICG. Furthermore, their photothermal properties were also notably strengthened, in which a wider functional pH range, 50% improvement in photothermal conversion efficiency and superior photothermal cyclability were achieved. Thanks to these superior properties, ICGCDs were demonstrated as efficient NIR bioimaging and photothermal agents in both *in vitro* and *in vivo* experiments. Most excitingly, the strategy demonstrated in this study is likely to have broad applications in other systems.

1. Introduction

Indocyanine green (ICG) is a type of tricarbocyanine dye, which has been clinically adopted for over 60 years since its approval by the United States Food and Drug Administration in 1959.[1] ICG has been widely used as a near-infrared (NIR) fluorescent contrast agent for many biomedical applications, such as sentinel lymph node mapping, angiography, assessment of hepatic dysfunction and oncology imaging.[2,3] In addition, ICG is also widely applied as photothermal therapy (PTT) agent due to its capability of converting absorbed NIR light into heat.[4] Despite these advantages, several limitations significantly restricted its wide application in the biomedical field, including poor chemical and optical stabilities,[5] concentration and time-dependent aggregation,[6] mediocre photothermal conversion efficiency (PCE) and short *in vivo* circulation time.[7,8] In this context, great efforts including chemical modification,[9] human serum albumin loading[10] and nano-micellization[11] have been devoted to overcoming these shortcomings. Nevertheless, these approaches generally included complicated processing or highly cytotoxic components, significantly limiting their practical applications. Thus, the development of simple strategies to enhance the stability and photothermal properties of ICG has attracted increasing attention.

On the other hand, carbon dots (C-dots) have attracted enormous interest in the biomedical fields due to their versatile synthesis and modification, excellent chemical stability, outstanding photoluminescence (PL) properties and photobleaching resistance.[12–15] Furthermore, C-dots demonstrated great biocompatibility and low-toxicity compared with traditional nanomaterials (*i.e.*, semiconductor quantum dots).[16,17] Most importantly, it seems that some of the original characteristic properties of the carbon precursors could be successfully preserved in the newly synthesized C-dots, endowing them with key functions.[18–22] In such context, it would be of great significance and necessity to explore whether the carbonization of traditional substances (*i.e.*, ICG) into C-dots could tackle the challenges that are hardly resolvable with traditional approaches. Specifically, we aimed to prepare ICG-derived C-dots (ICGCDs) *via* the carbonization of ICG that not only inherit the NIR emissions and photothermal capabilities but also obtain much-enhanced chemical, PL and biological properties. It's worth highlighting that if the above-mentioned aims could be successfully realized and further promoted to other systems, then it would give chemists and materials scientists powerful tools to treat certain types of carbon precursors (*i.e.*, dyes, small organic molecules, biomacromolecules, *etc.*) *via* simple carbonization to improve their chemical, PL and biological properties while still maintaining their unique characteristics.

[a]*Yunnan Key Laboratory for Micro/Nano Materials & Technology, School of Materials and Energy, Yunnan University, Kunming 650091, People's Republic of China. E-mail: zhilip@ynu.edu.cn; Tel: +86-871-65037399*

[b]*Yunnan Provincial Key Laboratory of Pharmacology for Natural Products, School of Pharmaceutical Sciences, Kunming Medical University, Kunming 650500, People's Republic of China. E-mail: jiayinnong@kmmu.edu.cn; Tel: +86-871-65922806*

†Electronic supplementary information (ESI) available. See DOI: https://doi.org/10.1039/d2nr06058b

‡These authors contributed equally to this work.

Herein, we reported here our latest finding in developing a simple carbonization strategy for the preparation of nanosized ICGCDs and their applications for both *in vitro* and *in vivo* PTT. Specifically, ICGCDs were fabricated by a one-step hydrothermal treatment from organic dye ICG and showed typical characteristics of C-dots. Significantly, not only the ICGCDs inherited the NIR emissions and photothermal capabilities of ICG, but they also demonstrated much improved chemical and photostability, anti-photobleaching capability and biocompatibility. Furthermore, the PCE of ICGCDs was enhanced by almost 50% compared to that of ICG. To the best of our knowledge, this is the first study in which simple carbonization of organic dyes could greatly enhance their properties in all aspects. In light of the excellent properties ICGCDs demonstrated, we also carried out a series of *in vitro* cellular studies, demonstrating ICGCDs as highly efficient bioimaging and photothermal agents with no noticeable cytotoxicity. Furthermore, tumor-bearing mice were treated with ICGCDs photothermally, which significantly inhibited the growth of tumors, highlighting the potential clinical application of ICGCDs for cancer treatment.

2. Materials and methods

2.1 Reagents and materials

ICG was purchased from Energy Chemical Reagent Co., Ltd (Shanghai, China). Fetal bovine serum (FBS) was obtained from Capricorn Scientific Co., Ltd (Hesse, Germany). Dulbecco's modified Eagle's medium (DMEM), minimum essential medium (MEM), trypsin and 1% penicillin/streptomycin were purchased from Life Technologies (Grand Island, NY, USA). 3-(4,5-Dimethyl-2-thiazolyl)-2,5-diphenyl-2*H*-tetrazolium bromide (MTT) was purchased from Sigma Co., Ltd (Shanghai, China). The reagents were used as received without further purification, unless otherwise noted. Deionized (DI) water used in all experiments was obtained from a Master Touch-S laboratory ultrapure water machine (Master Touch, Shanghai China).

2.2 Synthesis of ICGCDs

Briefly, ICG (30 mg) was dissolved in 10 mL of deionized water, and stirred well at 400 rpm for 2 h before the mixture was transferred to a 50 mL Teflon-lined autoclave and heated at 105 °C for 4 h. After cooling down, a blackish green mixture was obtained, which was centrifuged at 1500 rpm for 15 min, and then filtered through a 0.22 μm membrane to remove the residual large particles. The filtrate was collected in a dialysis bag (MWCO = 1000 Da) and dialyzed against DI water for three days, the resulting dispersions containing C-dots in the dialysis bag were then freeze-dried to yield the dark-green powders as the final products.

2.3 Characterizations of ICGCDs

The particle sizes of C-dots were measured on a transmission electron microscope (JEM-2100, JEOL, Japan) and the acceleration voltage was set at 200 kV. The TEM sample was prepared as follows: dispersions of ICGCDs (100 μg mL^{-1}) were added to the copper mesh drop by drop and allowed to dry naturally. Atomic force microscopy (AFM) was performed using a Park NX10 (Korea). The X-ray diffraction (XRD) pattern was obtained on an X-ray diffractometer (DX-2700BH, Haoyuan Instrument Co., Ltd, China) at a wavelength (λ) of 0.15406 nm. The Raman spectra were recorded on a Micro Confocal Raman spectrometer (InVia, Renishaw, England) with an excitation wavelength set at 785 nm. Ultraviolet-visible (UV-Vis) absorption spectra were recorded using an UV-Vis spectrophotometer (UV-2600, Shimadzu, Japan), where the wavelength range was set at 195–1100 nm, the scanning speed was set to medium, the sampling interval as 1 nm, and samplings were repeated twice. ICGCDs dispersions for measurements were 10 μg mL^{-1} in DI water. The fluorescence spectra were recorded using a fluorescence spectrometer (F97 Pro, Shanghai Prism Technology Co., Ltd, China). The scanning mode was set as three-dimensional wavelength scanning. The excitation and emission wavelengths were both set from 200 to 900 nm, with the width set as 10 nm. The scanning speed was 1000 nm min^{-1}, and the scanning interval was 1 nm; the gain was set as 650 V. The ICGCDs dispersions for measurements were 10 μg mL^{-1} in DI water. Fourier transform infrared (FTIR) spectra were recorded using an FTIR spectrometer (Middle Age Walker, Thermo, USA). The XPS spectra were obtained by X-ray photoelectron spectroscopy (K-Alpha$^+$, Thermo, USA), the X-ray source was monochromatic Al Kα with a $h\upsilon$ = 1486.6 eV photo energy operated at 6 mA × 12 kV.

2.4 Photothermal performance evaluation

The photothermal performance of ICG solutions and ICGCDs dispersions of different concentrations (5, 10, 20, 30, 40, 50, and 100 μg mL^{-1}) was measured under the irradiation of an 808 nm NIR laser (MDL-III-808-2.5 W, Changchun New Industries Optoelectronics Tech Co., Ltd, China). The temperatures of the solutions/dispersions under irradiation were measured using an infrared thermal camera (FLIR-E6390, USA) every 30 s for 10 min. In order to measure the photothermal conversion efficiency of ICGCDs, the aqueous dispersion of ICGCDs (50 μg mL^{-1}) was subjected to continuous irradiation until reaching a steady state and then the laser was turned off to allow the temperature to return back to r.t. naturally. The temperature variation of the solution in the whole process was recorded. The photothermal conversion efficiency (η) of ICGCDs was calculated according to the following equation:[23]

$$\eta = \frac{hS(T_{max} - T_{surr}) - Q_{dis}}{I(1 - 10^{-A_{808}})} \quad (1)$$

where h is the heat transfer coefficient, S is the surface area of the container, T_{max} is the steady-state temperature, T_{surr} is the room temperature, Q_{dis} is the heat dissipation from the light absorbed by the quartz sample cell, I is the laser power, and A_{808} is the absorbance of ICGCDs dispersions at 808 nm. The

value of h and S was calculated according to the following equation

$$\tau_s = \frac{m_D C_D}{hS} \quad (2)$$

where τ_s is the sample system time constant and m_D and C_D are the mass and heat capacity of DI water, respectively.

To investigate the influence of the laser power, ICG and ICGCDs aqueous solution/dispersion (50 μg mL^{-1}) were irradiated by a laser with different power densities (0.5, 1, 1.5, 2, 2.5 W cm^{-2}), each condition was irradiated for 10 min and the temperature was recorded every 30 s. In addition, to study the influence of pH, ICG and ICGCDs aqueous solutions/dispersions (50 μg mL^{-1}) of different pH values were irradiated by a laser (2.5 W cm^{-2}) for 10 min and the temperature was also recorded every 30 s.

2.5 Cell culture

The human keratinocyte (HaCaT) cell was cultured in MEM, containing 10% FBS and 1% penicillin/streptomycin. The human breast cancer cells MDA-MB-435 (435) cells were cultured in DMEM with 10% FBS and 1% penicillin/streptomycin. All the cells were cultured at 37 °C under a 5% CO_2 humidified atmosphere in a CO_2 incubator.

2.6 Cytotoxicity assay

The cell viability was measured by the MTT assay on HaCaT with the administration of ICG/ICGCDs. Generally, cells were seeded in 96-well plates with a final volume of 90 μL at a density of 3 × 10^3 cells per well and incubated at 37 °C in 5% CO_2 overnight. Then ICG/ICGCDs with different concentrations at a final volume of 10 μL were added to each well. After being incubated for 72 h, 10 μL MTT solution was added to each well and further incubated for 4 h. After that, the supernatant of each well was removed and 100 μL DMSO was added to each well. The plates were shaken for 15 min before analysis. Finally, the optical densities of the samples were recorded using a microplate reader (FC, Thermo, USA) at a wavelength of 570 nm.

2.7 Hemolysis assay

For sample preparation, 2 mL of fresh mouse blood was collected into a 15 mL heparin anticoagulant, which was then centrifuged at 1200 rpm for 15 min. After that, the supernatant was discarded and the cell precipitation was washed gently with PBS. The centrifugation was repeated until the supernatant was clear, then the precipitate was collected to obtain mouse red blood cells (MRBCs). Next, 1 mL of PBS was used to resuspend MRBCs and prepare samples for control and experiment group. Positive group: 100 μL of MRBCs and 900 μL of DI water. Negative control group: 100 μL of MRBCs and 900 μL of PBS. Experiment group: 100 μL of MRBCs and 900 μL of ICGCDs of different concentrations (50 μg mL^{-1}, 100 μg mL^{-1}, 200 μg mL^{-1} and 400 μg mL^{-1}). The samples of each group were incubated in a 37 °C water bath for 2 h, which was then centrifuged at 1500 rpm for 5 min. The absorbance at 541 nm of the supernatant of each group was measured using a UV-Vis spectrophotometer. The hemolytic rate of ICGCDs was calculated according to the following equation:

$$\text{Hemolysis}(\%) = \frac{A_{ICGCDs} - A_{negative}}{A_{positive} - A_{negative}} \quad (3)$$

where A_{ICGCDs}, $A_{positive}$ and $A_{negative}$ are the absorbance at 541 nm of supernatants of the experiment group, positive group and negative group, respectively.

2.8 Cell imaging

For sample preparation, 435 cells were seeded in 24-well plates containing 900 μL DMEM at a density of 1 × 10^5 cells per well and incubated for 24 h. Then 100 μL of ICGCDs dispersion (1 mg mL^{-1}) was added and further incubated for 4 h. The cells were then washed three times with PBS and fixed with 4% paraformaldehyde solution for 15 min, followed by another three times washing with l PBS. The fluorescence images were then obtained with an inverted fluorescence microscope (Ni-U, Nikon, Japan).

2.9 *In vitro* photothermal cytotoxicity

Firstly, 435 cells were seeded into 96-well plates at a density of 1 × 10^4 and incubated for 24 h. For the photothermal cytotoxicity study, ICG solutions and ICGCDs dispersions of various concentrations (0, 5, 10, 20, 40, 50 and 100 μg mL^{-1}) were added to the cells and incubated for another 4 h before they were irradiated with an 808 nm laser (2.5 W cm^{-2}, 8 min); for the control group, the cells were continuously incubated for 4 h at the dark without laser irradiation. After that, the cell viabilities were analyzed by MTT assays.

2.10 Tumor model for photothermal therapy

Animal care experiments and subsequent euthanasia were performed in accordance with the protocols approved by the Laboratory Animal Center of Kunming Medical University (kmmu2021198). Specifically, a 435 xenograft nude mice model was established by the injection of 435 cells to the nude mice (1 × 10^6 per mouse) subcutaneously. The tumor volume and mice weight were monitored daily until the volume of tumors in mice reached ~100 mm^3. After that, the mice were randomly separated into treatment and control groups. To investigate the *in vivo* PTT effect of ICGCDs, 70 μL of ICGCDs (1 mg mL^{-1}) were intratumorally injected into the mice. After 1 h, the mice were exposed to 808 nm NIR laser irradiation (1 W cm^{-2}) for 5 min. During the laser treatment, the infrared images were obtained by an infrared thermal camera. The tumor volume was calculated using the following formula

$$V = a \times b^2/2 \quad (4)$$

where a and b are the length and width of the tumors.

3. Results and discussion

3.1. Synthesis and characterization of ICGCDs

The ICGCDs reported in this study were synthesized through a one-pot hydrothermal process and various characterizations

have been applied to elucidate their structural, optical and chemical properties. Firstly, TEM was used to determine the morphology and structure of the as-prepared ICGCDs, as can be seen, ICGCDs were well dispersed spherical particles with no apparent aggregation (Fig. 1a). According to the particle size statistics, the diameters of these particles ranged from 1.41 to 4.37 nm, with an average size of 2.43 nm (Fig. 1a, lower left inset). The HRTEM image (Fig. 1a, upper right inset) of ICGCDs showed noticeable lattice fringes with a lattice spacing of 0.21 nm, which coincided with the (100) lattice of graphitic cores, indicating the successful carbonization and graphitization of the carbon precursors. Meanwhile, AFM revealed that the average height of ICGCDs was 2.60 nm, further picturing ICGCDs as quasi-spherical nanoparticles (Fig. 1b). Furthermore, XRD pattern of ICGCDs demonstrated a broad peak centered at 20.9°, which was commonly observed for C-dots and generally attributed to the crystalline graphite-like structure of the carbon core[24,25] (Fig. 1c). Compared to the sharp Raman spectra of ICG (Fig. S1†), ICGCDs showed broad peaks of D and G bands at 1350 and 1580 cm^{-1}, respectively, suggesting the successful carbonization of the raw materials. The low ratio of I_D/I_G (0.318) in the ICGCDs also supported the existence of highly ordered sp^2 clusters with few structural defects (Fig. 1d).

Next, we studied the optical properties of ICGCDs. The UV-Vis absorption spectrum of ICGCDs demonstrated an absorption peak at 215 nm corresponding to the π–π* transitions of C=C, which might be inherited from the carbon precursor ICG. Compared with the peaks at 717 and 779 nm of ICG, their counterparts of ICGCDs showed an apparent red shift to 780 and 895 nm, respectively, indicating the formation of larger conjugate structures during the carbonization process (Fig. 2a). Interestingly, the aqueous dispersion of ICGCDs was dark green under ambient light while the aqueous solution of ICG was bright green, which might be attributed to the influence of carbonization (Fig. 2a, inset). Different from the clean emissions of ICG (Fig. S2†), the PL emissions of ICGCDs were made up of three components (Fig. 2b). Peaks centered at 406 nm displayed the typical excitation-wavelength-dependent emission behavior, which shifted from 383 to 456 nm as the excitation wavelengths increased from 290 to 390 nm. On the other hand, the other two peaks centered at 600 and 697 nm, respectively, demonstrated excitation-independent emissions, which could be attributed to the homogeneous morphologies and surface chemical states of ICGCDs.[26] To our delight, the PL of ICGCDs was quite stable across a wide range of pH (pH = 2–11, Fig. S3†).

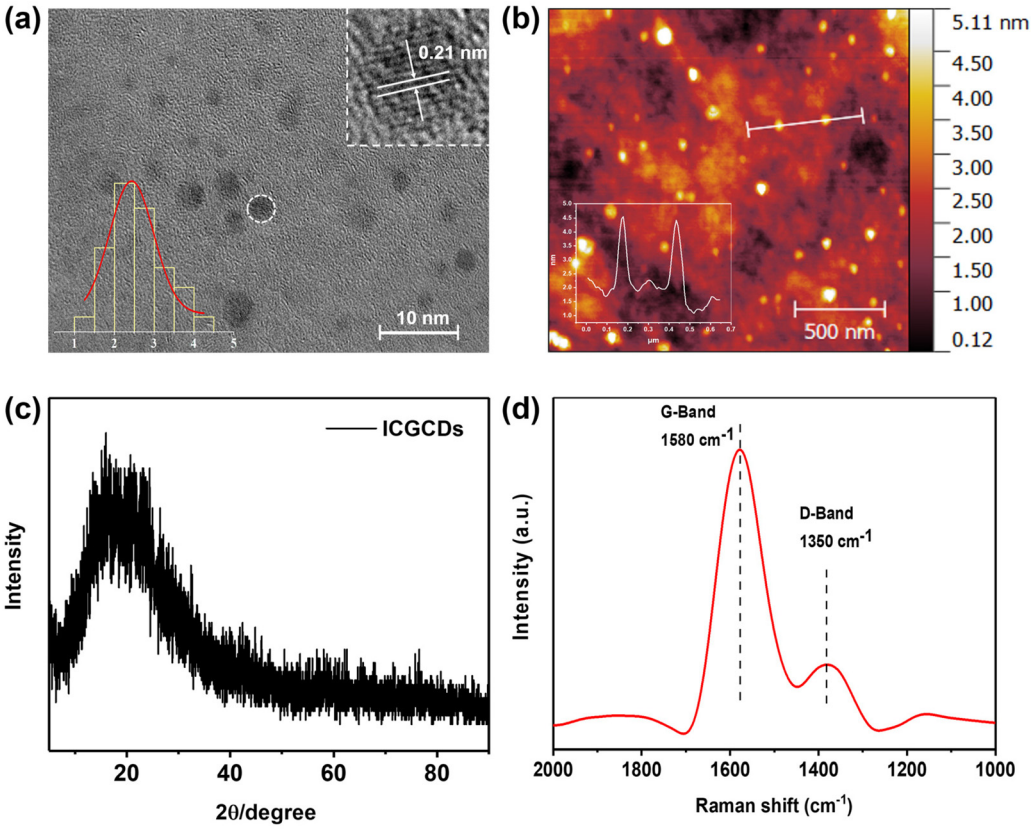

Fig. 1 (a) TEM images of ICGCDs, the upper right inset is the enlarged picture of the specific particle, while the lower inset is the corresponding size distribution histograms of the particles. (b) AFM images of ICGCDs, the inset shows the height profiles analysis. (c) XRD pattern of ICGCDs. (d) Raman spectra of ICGCDs.

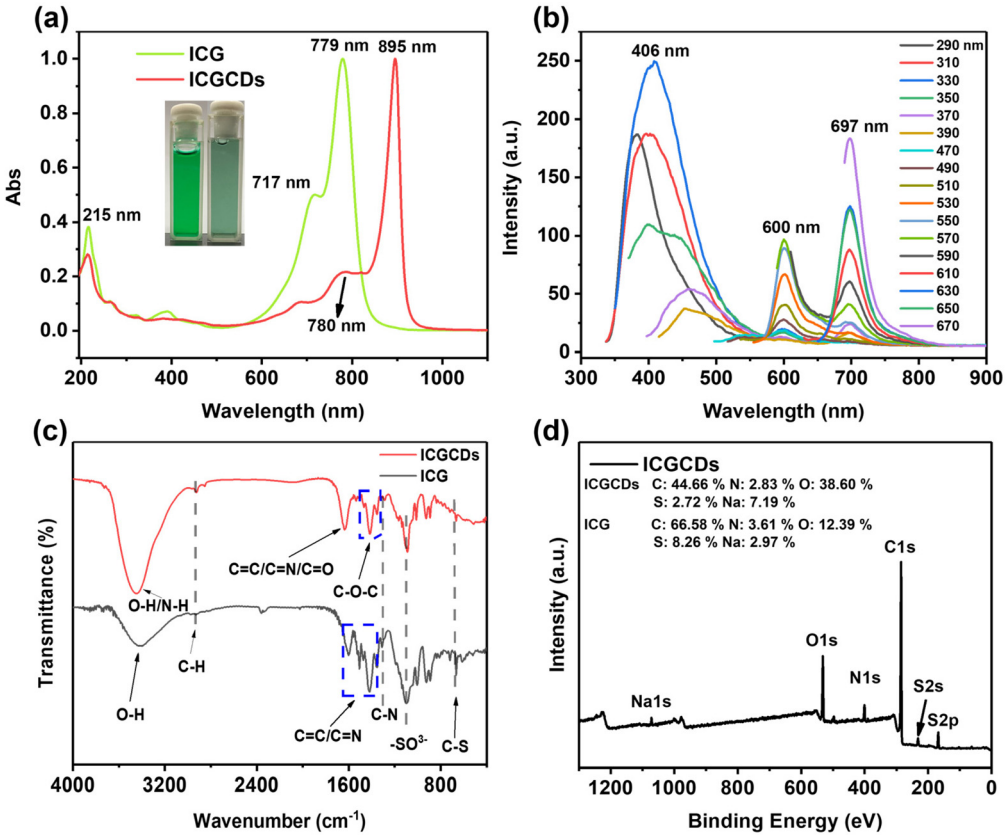

Fig. 2 (a) UV-Vis absorption spectra of ICG and ICGCDs, inset photographs showing ICG (left) and ICGCDs (right) under ambient light. (b) The fluorescence emission spectrum of ICGCDs. (c) FTIR spectra of ICG and ICGCDs. (d) XPS survey spectrum of ICGCDs.

Following the optical properties, we then compared the chemical composition of ICG and ICGCDs determined by FTIR and XPS. In the FTIR spectrum of ICG (Fig. 2c), the broad peak at 3412 cm^{-1} was attributed to the O–H stretching vibration, whereas the peaks at 2935, 1417–1606 and 1311 cm^{-1} could be assigned to the stretching vibrations of C–H, C═C/C═N and C–N, respectively. The bands at 1094 and 667 cm^{-1} depicted $–SO^{3-}$ bonds and bending vibration of C–S. On the other hand, peaks at 3453, 2924 and 1295 cm^{-1} are shown in the FTIR spectra of ICGCDs, which were assigned to the stretching vibrations of O–H/N–H, C–H and C–N, respectively. Interestingly, ICGCDs demonstrated identical peaks at 1094 and 667 cm^{-1}, indicating they might have inherited the identical functional group ($–SO^{3-}$) from ICG. Notably, new peaks at 1330–1492 cm^{-1} and 1632 cm^{-1} appeared, which could be attributed to the stretching vibrations of C–O–C and C═O, respectively, indicating a certain degree of oxidized decomposition and carbonization occurred during the hydrothermal process.

In addition to FTIR, the chemical composition of ICGCDs was further characterized by XPS. According to the full scan survey spectra, it is clear that ICGCDs contained carbon (around 284 eV), nitrogen (around 400 eV), oxygen (around 531 eV), sulfur (around 168 eV) and sodium (1072 eV), which were in high accordance with the elemental composition of ICG (Fig. 2d). As expected, the oxygen contents of ICGCDs increased from 12.39% for ICG to 38.60% while the carbon and sulfur contents of ICGCDs decreased from 66.58 and 8.26% for ICG to 44.66 and 2.72%, respectively, indicating that significant amounts of carbon and sulfur have been replaced by oxygen during the preparation of ICGCDs (Fig. 2d, inset). On the other hand, the contents of nitrogen remained very similar for ICG and ICGCDs.

The high-resolution C 1s spectrum could be fitted to four binding energies: C–C/C═C (248.8 eV), C–N/C–S (285.2 eV), C–O (286.5 eV) and C═O/C═N (287.8 eV) (Fig. S4a†). The N 1s spectrum could be deconvoluted into three peaks corresponding to the pyridinic (399.7 eV), pyrrolic (400.6 eV) and amide N (402.2 eV) (Fig. S4b†). As shown in the O 1s spectrum (Fig. S4c†), two peaks at 531 and 532.3 eV could be attributed to the C═O and C–O–C/C–OH, respectively. The S 2p could be deconvoluted into three components at 166.8, 168.1 and 169.7 eV, which were associated with $–C\text{-}SO_x–$ (x = 2, 3, 4) species such as sulfate or sulfonate (Fig. S4d†). Finally, the zeta potential of ICG was −32.8 mV (Fig. S5a†) while that of ICGCDs was determined to be −15.8 mV (Fig. S5b†), the zeta potential shift of ICGCDs might be attributed to the loss of sulfate groups after the carbonization. In conclusion, we have successfully synthesized ICGCDs *via* the simple carbonization of ICG. ICGCDs demonstrated typical properties of C-dots and successfully inherited the NIR emission of ICG.

3.2. Comparison of ICG and ICGCD properties

In this study, ICG was selected as the carbon precursor for the preparation of highly efficient NIR C-dots. As a well-established NIR organic dye, ICG has been widely used as bioimaging and PTT agent for its NIR PL emissions and photothermal capability. Unfortunately, ICG frequently suffered from low chemical and optical stability, undesired aggregation, relatively inefficient PCE and short *in vivo* circulation time. As such, this study aimed to conquer these challenges *via* the simple carbonization of ICG to form ICGCDs, which could inherit the intrinsic NIR emissions and photothermal capabilities of ICG while having much enhanced optical stabilities, increased anti-photobleaching and strengthened photothermal properties compared to ICG (Fig. 3). In addition, the biocompatibility of ICGCDs was also expected to be improved as the carbonization could generally reduce the cytotoxicity of raw materials.

To explore whether carbonization of ICG did enhance the properties as planned, the properties of ICG and ICGCDs were systematically compared. The optical stabilities of ICG and ICGCDs under different temperatures were firstly investigated. Similar to previous studies,[27] the PL stability of ICG was quite weak (Fig. 4a, black lines). Specifically, the PL intensities of ICG solution began to decline since time zero and there was a 25% of intensity ablation after 15 h of storage under ambient conditions (23 °C). What's worse, when the temperature increased to normal body temperature (37 °C), the PL intensity of ICG decayed much more rapidly, losing almost 90% of the initial intensity in the first 3 h, which greatly limited the in-depth applications of ICG in the biomedical fields. When the temperature was further elevated to 60 °C, it quickly lost 93%

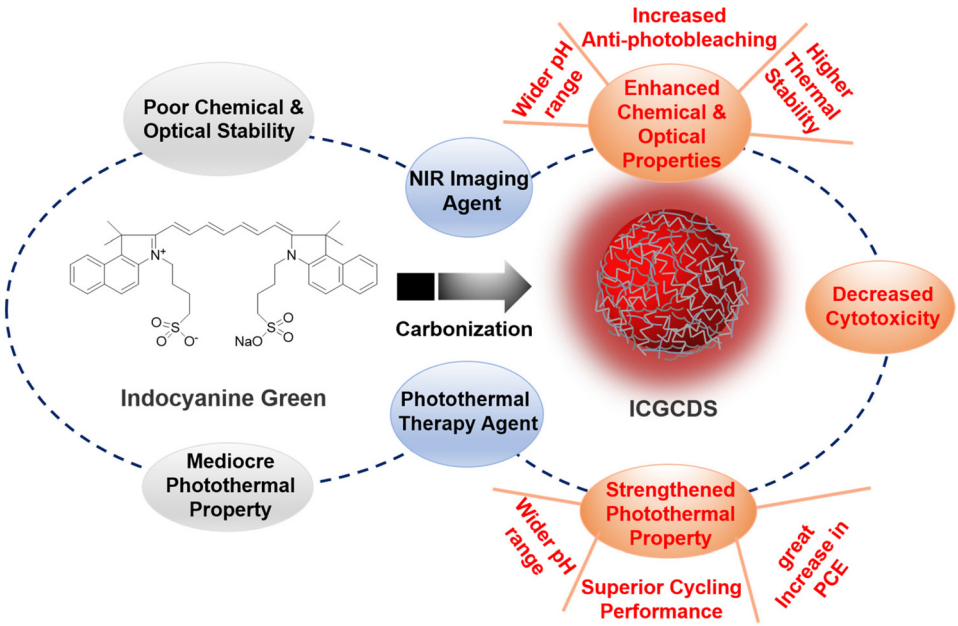

Fig. 3 Experimental design idea of this study: to prepare ICGCDs *via* the simple carbonization of ICG, which not only inherit the characteristics (*i.e.*, NIR emissions, photothermal capability) of ICG, but also refrain from its shortcomings (*i.e.*, poor chemical and optical stability, mediocre photothermal properties). PCE: photothermal conversion efficiency; ICGCDs: indocyanine green-derived carbon dots.

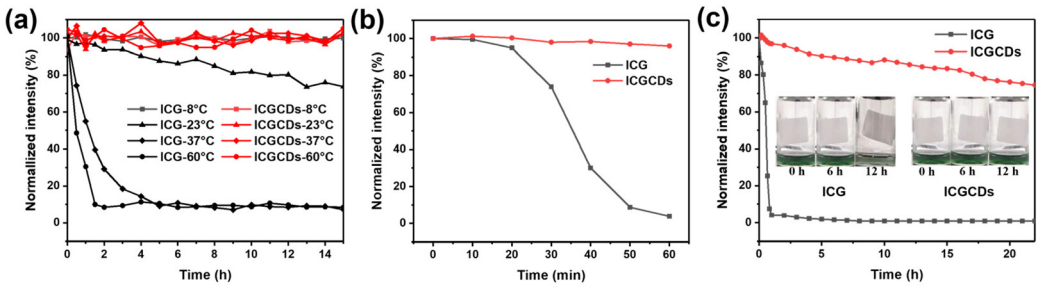

Fig. 4 (a) The normalized fluorescence emission intensities of ICG and ICGCDs at different temperatures. The normalized fluorescence emission intensities of ICG and ICGCDs under continuous irradiation by a xenon lamp (500 W, 300–1100 nm): (b) irradiation for 1 h and (c) irradiation for 22 h, the insets are the pictures of ICG solutions (left) and ICGCDs dispersions (right) after continuous irradiation for the respective time as indicated.

of the PL intensity in the first 2 h. As can be seen, the PL of ICG demonstrated acceptable stability only when the temperature was decreased to −8 °C (Fig. 4a, black lines), which is not practical for actual applications. To our delight, the carbonization of ICG to ICGCDs has significantly enhanced the PL stabilities. As demonstrated, the PL intensities of ICGCDs had no noticeable decays at all the temperatures tested (Fig. 4a, red lines), indicating that the strategy applied in this study is indeed feasible and promising!

In addition to the normal PL stability improvement, to our delight, the photobleaching resistance ability of ICGCDs was also significantly enhanced. As can be seen, the PL intensity of ICG decayed dramatically to 4.0% after 60 min of continuous irradiation by a xenon lamp (500 W, 300–1100 nm) while that of ICGCDs remained virtually unchanged (Fig. 4b). Moreover, ICGCDs demonstrated a high level of anti-photobleaching even after 22 h of continuous irradiation (Fig. 4c, red line), highlighting the potential of ICGCDs as an excellent imaging agent for long-term, continuous tracking. It is worth mentioning that the differences in their anti-photobleaching abilities could also be visually distinguished based on the aqueous solution/dispersion of ICG and ICGCDs. As shown, the greenish aqueous solution of ICG turned to colorless after 12 h of irradiation (Fig. 4c, left inset), possibly due to the degradation of ICG while no evident change was observed for the aqueous dispersion of ICGCDs (Fig. 4c, right inset).

Apart from their NIR emission, ICG is also known for its intrinsic photothermal properties. As such, we also paid extra attention to the photothermal performances of ICG and ICGCDs. As demonstrated, ICG had a good photothermal ability that was concentration-dependent (Fig. 5a). Specifically, when the concentration was low (*i.e.*, 10 μg mL^{-1}), there was no noticeable difference between the sample and PBS buffer (Fig. 5a, red curve *vs.* black curve). Starting from 20 μg mL^{-1}, the photothermal effects of ICG became obvious and enhanced as the concentration increased, resulting in a 45.5 °C temperature increase as the concentration of ICG reached 100 μg mL^{-1} (Fig. 5a, cyan curve). Unfortunately, samples with high concentrations (40–100 μg mL^{-1}) showed declined temperatures after 400 s of continuous irradiation, which might be attributed to the unstable nature and self-photothermal decomposition of ICG. On the other hand, to our surprise, not only the intrinsic photothermal property of ICG was inherited by ICGCDs, but also it was greatly enhanced! ICGCDs, unlike ICG, demonstrated high degree of photothermal effects even at very low concentrations (*i.e.*, 5 and 10 μg mL^{-1}, Fig. 5b, red and blue curves). As the concentrations increased, the photothermal effects of ICGCDs were also quickly enhanced, achieving a maximum of 65.7 °C temperature increase as the concentration was set at 100 μg mL^{-1} (Fig. 5b, brown curve). Most importantly, unlike ICG, there was no sign of temperature decline after 600 s of continuous laser irradiation for all the concentrations tested, demonstrating the superior photothermal stability of ICGCDs (Fig. 5b). Besides, the dispersion of ICGCDs (50 μg mL^{-1}) also demonstrated laser power-dependent photothermal effects (Fig. S6†), which could be exploited to fine tune the temperature elevation of the system. As demonstrated, due to their excellent photothermal efficiency, ICGCDs achieved much higher temperature increase than ICG at all concentrations tested (Fig. 5c). To

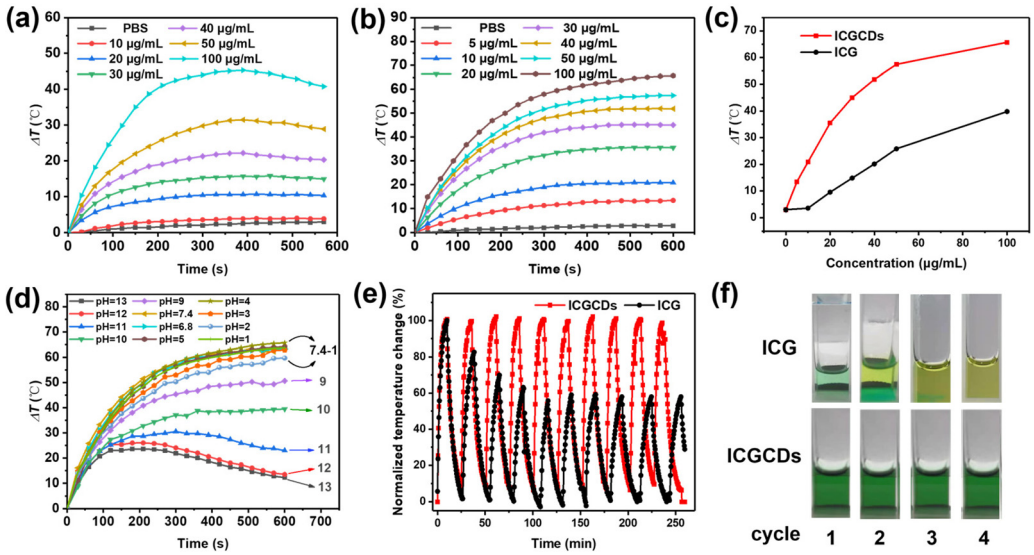

Fig. 5 Temperature variations of (a) ICG solutions and (b) ICGCD dispersions of different concentrations after irradiated with an 808 nm laser (2.5 W cm^{-2}). (c) Plot of temperature changes (ΔT) *versus* concentrations of ICG solutions and ICGCDs dispersions after 10 min of laser irradiation. (d) Temperature variations of ICGCDs dispersion (50 μg mL^{-1}) under different pH. (e) Cyclability test for ICG solution and ICGCDs dispersion (50 μg mL^{-1}) under repeated laser irradiations (808 nm, 2.5 W cm^{-2}): black and red curves represent the temperature variations for ICG and ICGCDs, respectively, over 10 on/off cycles. The rising parts of the curves correspond to the laser irradiation (laser on) while the descending parts of the curves correspond to the natural cooling (laser off). (f) Photos showing the aqueous solution of ICG (top) and dispersion of ICGCDs (bottom) over 4 on/off cycles of 808 nm laser (2.5 W cm^{-2}) irradiation.

quantitatively compare their photothermal effects, the PCEs of ICG and ICGCDs (50 μg mL^{-1}) were determined according to well-established procedures[28,29] (Fig. S7†). The PCE of ICGCDs was calculated to be 23.9%, which is much higher than that of ICG (16.3%), achieving almost 50% enhancement! The origin of the photothermal ability of ICGCDs could be ascribed to the inheritance of the intrinsic characteristics of carbon precursor ICG, as methyl cyanine dyes are well known for their photothermal capacity.[30] After successful carbonization, ICGCDs might be regarded as the nanoscale formulation of cyanine dyes, which may have effectively avoided the intense aggregation of ICG and thus reduced the dissipation of excited-state energy through radiative relaxation, leading to a much enhanced PCE.[31]

In addition to the enhanced PCE discussed above, to our delight, the pH scope and cyclability of ICGCDs were also greatly improved. Compared with the very limited functional pH range of ICG (Fig. S8†), ICGCDs demonstrated a much broader functional pH range from 1 to 7.4 (Fig. 5d), which included both the pH environments of normal tissues (pH = 7.2–7.4) and various solid tumors (pH < 7),[32] making ICGCDs much more competitive than ICG as potential agents for *in vivo* PTT. Furthermore, ICGCDs also performed much better in the cyclability test than ICG. Under repeated laser irradiation, ICGCDs maintained essentially the same PCE even after 10 cycles as indicated by the unaltered temperature peaks (Fig. 5e, red curves) while the photothermal performances of ICG began to quickly deteriorate since the second cycle, and only 57.3% of the original PCE was retained in the fifth cycle (Fig. 5e, black curves). The stability differences of ICG and ICGCDs in the cyclability test could also be visually differentiated, in which the greenish color of the ICG solution quickly faded away in the first few cycles while that of ICGCDs remained essentially unchanged (Fig. 5f). In conclusion, carbonization of ICG into ICGCDs indeed enhanced their properties in all aspects, highlighting the high feasibility of the strategy proposed in this study.

3.3. Applications of ICGCDs: bioimaging and PTT

In light of their excellent PL and photothermal properties, the potential applications of ICGCDs for bioimaging and PTT were also demonstrated. To begin with, we evaluated the cytotoxicity of ICGCDs using normal HaCaT cells as the cell model. To our delight, the biocompatibility of ICGCGs was greatly enhanced compared to ICG, in which ICGCDs exhibited extremely low cytotoxicity compared to ICG at all concentration levels tested (Fig. S9†). Furthermore, the hemocompatibility of ICGCDs was tested to verify the feasibility of their application *in vivo*. As demonstrated (Fig. S10†), after incubation with red blood cells, the absorptions at 541 nm of ICGCD groups of different concentrations were all at low levels compared to the positive control group (Fig. S10a†). No obvious hemolysis was observed even when the concentration of ICGCDs was increased to 400 μg mL^{-1} (Fig. S10b†). The low hemolysis rate indicated that ICGCDs had great hemocompatibility and could be applied for *in vivo* applications.

Feasibility of ICGCDs as a bioimaging agent was then demonstrated using 435 cells as the cell model. Clearly, the cells treated with ICGCDs maintained their normal morphologies (Fig. 6a) and cells with strong red fluorescence could be easily observed under the excitation of a 525 nm channel (Fig. 6b). The red fluorescence could be attributed to the main emissions of ICGCDs above 600 nm, and showed no sign of deterioration after long periods of continuous excitation, demonstrating the high photostability of ICGCDs. Similarly, strong green (Fig. 6c) and blue (Fig. 6d) fluorescence emissions could be observed when excited under 470 and 385 nm excitation lights, respectively. Under higher magnification (Fig. 6b2–d2), we could see that the cytoplasm showed weak fluorescence whereas the fluorescence around the membranes was much stronger, indicating that the ICGCDs might be efficiently taken up by the 435 cells *via* the membrane-mediated endocytosis process.[33]

To investigate the photothermal cytotoxicity of ICGCDs on cancer cells, 435 cells were treated with ICGCD dispersions of different concentrations before they were irradiated with an 808 nm laser. Control experiments (without laser irradiation) show that the 435 cells maintained high viability, specifically, over 90% of viability was retained even in the presence of 100 μg mL^{-1} ICGCDs (Fig. 6e, black columns). However, the viability of 435 cells was significantly decreased under laser irradiation (Fig. 6e, red columns), demonstrating the high *in vitro* photothermal efficiency of ICGCDs. Notably, nearly 90% of 435 cells were killed with the presence of only 20 μg mL^{-1} ICGCDs under irradiation, which was better than most reported studies.[28,29,34,35] On the other hand, ICG demonstrated evident cytotoxicity at higher concentrations in the control experiments (Fig. 6f, black columns), which was in accordance with the cytotoxicity study discussed above. Furthermore, their photothermal efficiency was also much lower (Fig. 6f, red columns), only 35% of 435 cells cultured with 20 μg mL^{-1} of ICG were killed under laser irradiation while that for ICGCDs was 90%. These results clearly show that the biocompatibility and *in vitro* photothermal capability of ICG were significantly enhanced as they were carbonized and transformed into ICGCDs.

Encouraged by the wet and *in vitro* experiments, we further evaluated the photothermal therapeutic effects of ICGCDs *in vivo* using tumor-bearing mice as the model. Specifically, mice intratumorally injected with ICGCDs (PTT group) were irradiated with an 808 nm laser (1 W cm^{-2}) continuously for 5 min and an infrared thermal camera was used to monitor the whole process. As expected, the temperature of the tumor site for the PTT group was significantly elevated from 37.9 °C at 0 min to 63.7 °C at 5 min (ΔT = 25.8 °C) while that of the saline group only increased by 6.1 °C (Fig. 7a), demonstrating the excellent *in vivo* photothermal capability of ICGCDs. Excitingly, the tumor growth of the PTT group mice was significantly inhibited after only one photothermal treatment, and only a small black scar was left 14 days after the treatment (Fig. 7b1). In contrast, the other three control groups, including ICGCDs groups

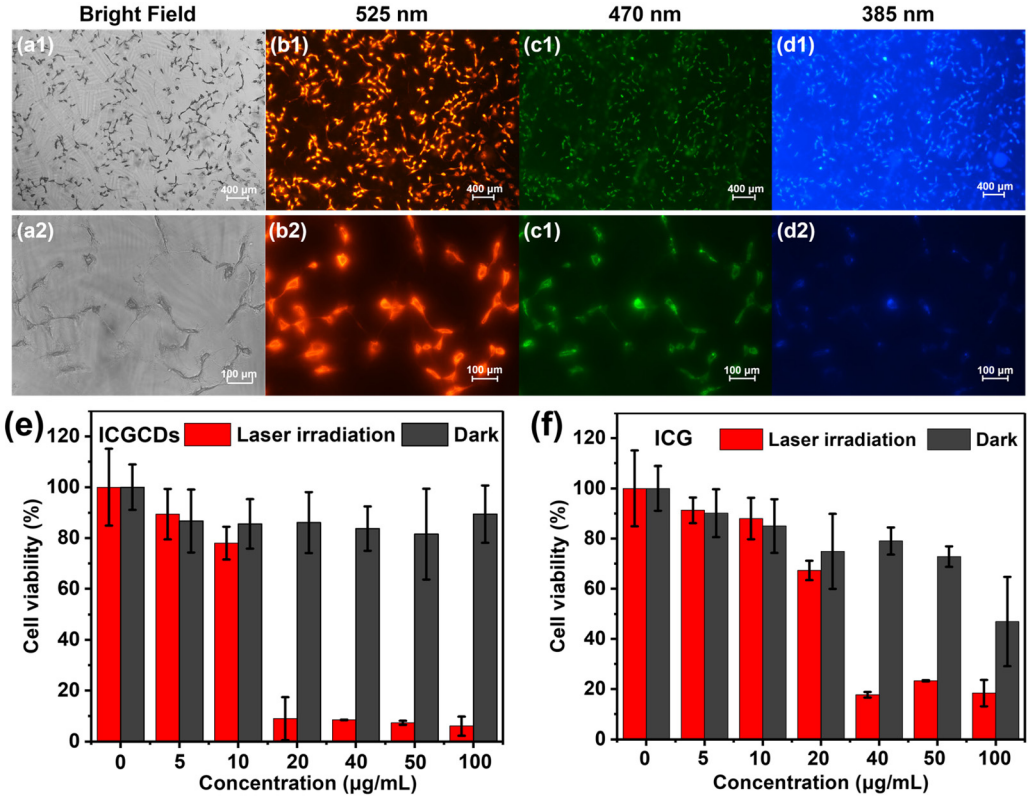

Fig. 6 The fluorescence images under (a1 and a2) bright field, (b1 and b2) 525 nm excitation, (c1 and c2) 470 nm excitation and (d1 and d2) 385 nm excitation of 435 cells incubated with ICGCDs for 4 h. The cell viability of 435 cells incubated with different concentrations of (e) ICGCDs or (f) ICG and irradiated with the 808 nm laser (2.5 W cm^{-2}, 8 min).

without laser irradiation (Fig. 7b2), saline groups with laser irradiation (Fig. 7b3) and saline groups without laser irradiation (Fig. 7b4) did not suppress tumor growth at all. To quantitatively compare the tumor growths in different groups, the tumor volumes were monitored by an electronic vernier caliper every other day for 14 days (Fig. 7c). As observed, the tumor sizes of the PTT group mice did not show obvious shrinking in the first 10 days, which was due to the interference of the black scab at the tumor sites due to the PTT effect (Fig. S11†). The scabs began to desquamate after 10 days, and we were able to measure the tumor volumes much accurately; as shown, the tumor sizes of the PTT group reduced by almost 70% in the end after only one photothermal treatment (Fig. 7c, green line).

On the other hand, the tumors of the control groups all had significant growth: the ICGCDs group without laser irradiation increased 268.7% (Fig. 7c, blue line), saline groups with laser irradiation increased 219.1% (Fig. 7c, red line) and saline groups without laser irradiation increased 218.4% (Fig. 7c, black line). Moreover, the body weights for all the mice were monitored and showed no abnormality during the entire treatment (Fig. 7d), indicating that the photothermal treatment of ICGCDs did not alter the body functions of the mice, which highlighted the excellent *in vivo* biocompatibility of the ICGCDs.

In addition to the direct measurement of the tumor volumes, an indirect approach was also taken to evaluate the development of the tumors after the photothermal treatments. It is well known that the occurrence and development of cancers are generally accompanied by the increase of immune cells[29] as the body is fighting back. Thus, the number of immune cells under similar body conditions could be used to roughly evaluate the degree of cancer development; the more immune cells, the more severe the cancers. As such, we carried out the blood analysis of the mice 14 days after the initial photothermal treatment. As expected, the immune cells including white blood cells (Fig. 7e), lymph cells (Fig. 7f) and neutrophil cells (Fig. 7g) of the PTT group were much lower than those of the control group (saline + laser irradiation). These results indicated that the tumor growth for the PTT group was indeed effectively inhibited; further demonstrating the excellent photothermal tumor ablation efficiency of ICGCDs. Moreover, major organs of the mice (heart, liver, spleen, lungs and kidneys) in the PTT group (Fig. 7h, top), saline group with laser irradiation (Fig. 7h, bottom), ICGCDs group without laser irradiation (Fig. S12a†) and saline group without laser irradiation (Fig. S12b†) were harvested and stained with H&E. No obvious toxicity was observed in the mice tissues, again demonstrating the high *in vivo* biocompatibility of the ICGCDs.

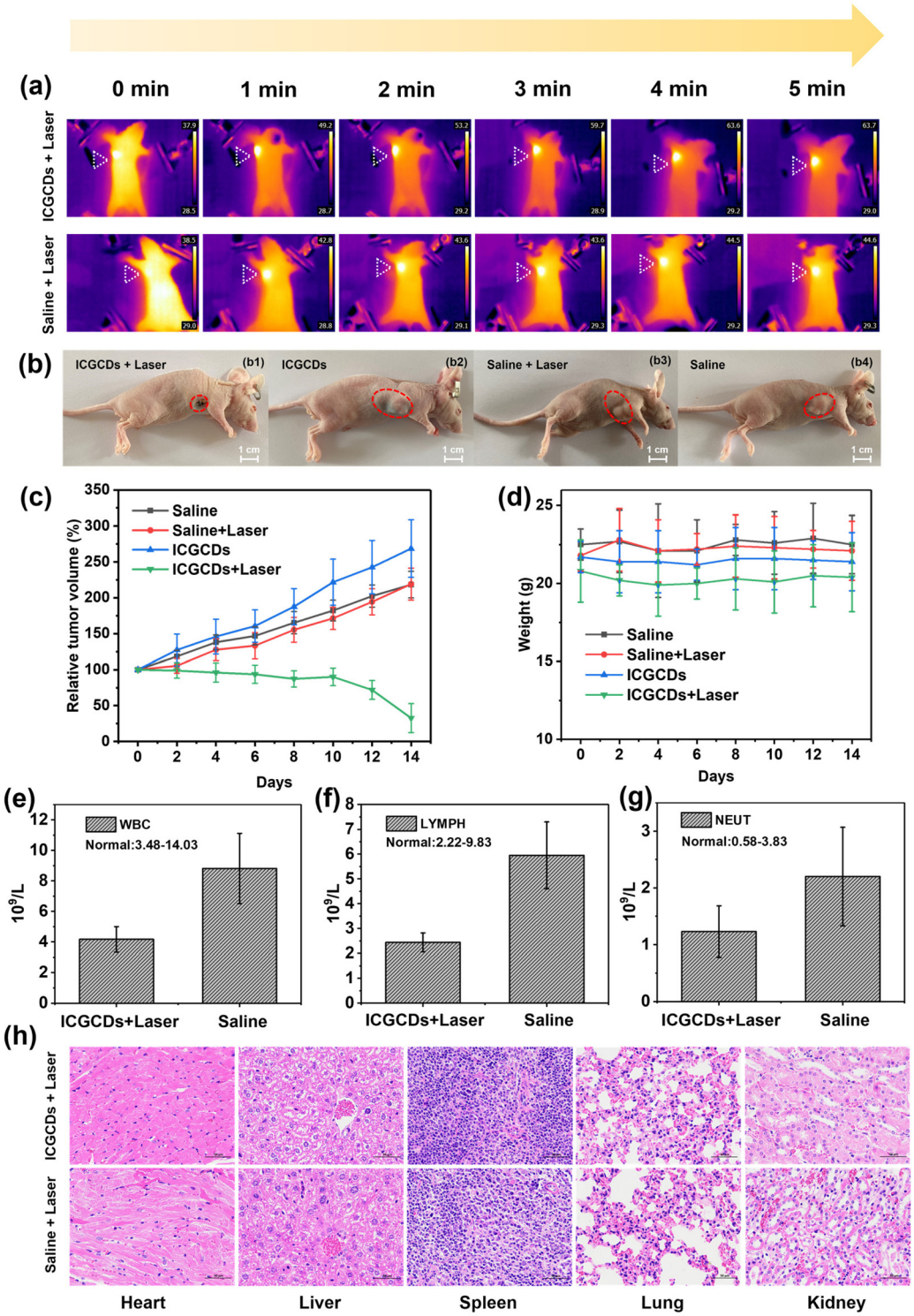

Fig. 7 (a) IR thermal images of the tumor-bearing mice treated with ICGCDs and saline under an 808 nm laser irradiation (1 W cm^{-2}, 5 min). (b) Photos of tumor-bearing mice two weeks after photothermal treatments: (b1) PTT group, ICGCDs with laser irradiation; (b2) ICGCDs without laser irradiation; (b3) saline with laser irradiation; and (b4) saline without laser irradiation. Initial sizes of the tumors of the mice varied slightly. (c) Relative tumor growth rate and (d) body weight of each treatment group monitored two weeks after photothermal treatment. Analysis of immune cells of the photothermal treated tumor-bearing mice *via* blood testing: (e) WBC, (f) LYMPH and (g) NEUT. (h) H&E staining of tissues from mice treated with ICGCDs and saline under laser irradiation (808 nm, 1 W cm^{-2}, 5 min).

4. Conclusion

In summary, a facile hydrothermal method was applied for the preparation of ICGCDs from traditional organic dye ICG. Careful characterizations revealed that ICGCDs possessed quasi-spherical morphology and demonstrated all the properties typically seen for C-dots. Significantly, ICGCDs exhibited much-enhanced chemical and optical properties compared to ICG, which greatly extended their application as the NIR imaging agent. Moreover, the photothermal properties of ICGCDs were notably strengthened compared to that of ICG, in which wider functional pH range, 50% improvement in PCE and superior photothermal cyclability were achieved. In light of the excellent photothermal properties of ICGCDs, their applications as efficient photothermal agents for both *in vitro* and *in vivo* PTT were demonstrated. These studies manifested that the strategy to enhance the properties of ICG *via* their carbonization into ICGCDs (Fig. 3) was indeed feasible and effective. Most prominently, considering its easy operation and simple validations, the strategy demonstrated in this study is likely to be promoted to other systems,[36,37] rendering chemists and materials scientists alternative yet powerful tools to tackle similar challenges.

Conflicts of interest

The authors declare that they have no known competing financial interests or personal relationships that could have appeared to influence the work reported in this paper.

Acknowledgements

Z. Peng and Y. Jia gratefully acknowledge the financial support from the National Natural Science Foundation of China under the grant numbers 21807010 and 82160344, and the Applied Basic Research Program of Yunnan Province under the grant numbers 2019FB066, 202001AU070141 and 202101AY070001-068. The authors thank the Advanced Analysis and Measurement Center of Yunnan University for the sample testing service.

References

1 J. A. Zelken and A. P. Tufaro, Current trends and emerging future of indocyanine green usage in surgery and oncology: An update, *Ann. Surg. Oncol.*, 2015, **22**, S1271–S1283.
2 L. van Manen, H. J. M. Handgraaf, M. Diana, J. Dijkstra, T. Ishizawa, A. L. Vahrmeijer and J. S. D. Mieog, A practical guide for the use of indocyanine green and methylene blue in fluorescence-guided abdominal surgery, *J. Surg. Oncol.*, 2018, **118**(2), 283–300.
3 J. T. Alander, I. Kaartinen, A. Laakso, T. Patila, T. Spillmann, V. V. Tuchin, M. Venermo and P. Valisuo, A review of indocyanine green fluorescent imaging in surgery, *Int. J. Biomed. Imaging*, 2012, **2012**, 940585–940585.
4 Z. Li, Q. Yin, B. Chen, Z. Wang, Y. Yan, T. Qi, W. Chen, Q. Zhang and Y. Wang, Ultra-ph-sensitive indocyanine green-conjugated nanoprobes for fluorescence imaging-guided photothermal cancer therapy, *Nanomedicine*, 2019, **17**, 287–296.
5 L. Yang, B. Huang, S. Hu, Y. An, J. Sheng, Y. Li, Y. Wang and N. Gu, Indocyanine green assembled free oxygen-nanobubbles towards enhanced near-infrared induced photodynamic therapy, *Nano Res.*, 2022, **15**(5), 4285–4293.
6 M. K. Ruhi, A. Ak and M. Gulsoy, Dose-dependent photochemical/photothermal toxicity of indocyanine green-based therapy on three different cancer cell lines, *Photodiagn. Photodyn. Ther.*, 2018, **21**, 334–343.
7 M. B. Reinhart, C. R. Huntington, L. J. Blair, B. T. Heniford and V. A. Augenstein, Indocyanine green: Historical context, current applications, and future considerations, *Surg. Innovation*, 2016, **23**(2), 166–175.
8 L. Yang, B. Huang, S. Q. Hu, Y. An, J. Y. Sheng, Y. Li, Y. X. Wang and N. Gu, Indocyanine green assembled free oxygen-nanobubbles towards enhanced near-infrared induced photodynamic therapy, *Nano Res.*, 2022, **15**(5), 4285–4293.
9 I. Mohammad, C. Stanford, M. D. Morton, Q. Zhu and M. B. Smith, Structurally modified indocyanine green dyes. Modification of the polyene linker, *Dyes Pigm.*, 2013, **99**(2), 275–283.
10 K. Kanazaki, K. Sano, A. Makino, A. Takahashi, J. Deguchi, M. Ohashi, T. Temma, M. Ono and H. Saji, Development of human serum albumin conjugated with near-infrared dye for photoacoustic tumor imaging, *J. Biomed. Opt.*, 2014, **19**(9), 096002.
11 A. Makino, S. Kizaka-Kondoh, R. Yamahara, I. Hara, T. Kanzaki, E. Ozeki, M. Hiraoka and S. Kimura, Near-infrared fluorescence tumor imaging using nanocarrier composed of poly(l-lactic acid)-block-poly(sarcosine) amphiphilic polydepsipeptide, *Biomaterials*, 2009, **30**(28), 5156–5160.
12 H. Li, Z. Kang, Y. Liu and S.-T. Lee, Carbon nanodots: Synthesis, properties and applications, *J. Mater. Chem.*, 2012, **22**(46), 24230–24253.
13 C. Zhao, Y. Jiao, F. Hu and Y. Yang, Green synthesis of carbon dots from pork and application as nanosensors for uric acid detection, *Spectrochim. Acta, Part A*, 2018, **190**, 360–367.
14 C. Y. Ji, Q. R. Han, Y. Q. Zhou, J. J. Wu, W. Q. Shi, L. P. Gao, R. M. Leblanc and Z. L. Peng, Phenylenediamine-derived near infrared carbon dots: The kilogram-scale preparation, formation process, photoluminescence tuning mechanism and application as red phosphors, *Carbon*, 2022, **192**, 198–208.
15 H. Li, S. Ye, J. Q. Guo, H. B. Wang, W. Yan, J. Song and J. L. Qu, Biocompatible carbon dots with low-saturation-intensity and high-photobleaching-resistance for sted nanoscopy imaging of the nucleolus and tunneling nanotubes in living cells, *Nano Res.*, 2019, **12**(12), 3075–3084.

16 Y. Morimoto, M. Horie, N. Kobayashi, N. Shinohara and M. Shimada, Inhalation toxicity assessment of carbon-based nanoparticles, *Acc. Chem. Res.*, 2013, **46**(3), 770–781.
17 C. Y. Ji, Y. Q. Zhou, R. M. Leblanc and Z. L. Peng, Recent developments of carbon dots in biosensing: A review, *ACS Sens.*, 2020, **5**(9), 2724–2741.
18 M. Zheng, Y. Li, S. Liu, W. Wang, Z. Xie and X. Jing, One-pot to synthesize multifunctional carbon dots for near infrared fluorescence imaging and photothermal cancer therapy, *ACS Appl. Mater. Interfaces*, 2016, **8**(36), 23533–23541.
19 I. K. Deshapriya, B. S. Stromer, A. Pattammattel, C. S. Kim, R. Iglesias-Bartolome, L. Gonzalez-Fajardo, V. Patel, J. S. Gutkind, X. L. Lu and C. V. Kumar, Fluorescent, bioactive protein nanoparticles (prodots) for rapid, improved cellular uptake, *Bioconjugate Chem.*, 2015, **26**(3), 396–404.
20 Y. Li, X. H. Zheng, X. Y. Zhang, S. Liu, Q. Pei, M. Zheng and Z. G. Xie, Porphyrin-based carbon dots for photodynamic therapy of hepatoma, *Adv. Healthcare Mater.*, 2017, **6**(1), 1600924.
21 S. K. Bhunia, A. R. Maity, S. Nandi, D. Stepensky and R. Jelinek, Imaging cancer cells expressing the folate receptor with carbon dots produced from folic acid, *ChemBioChem*, 2016, **17**(7), 614–619.
22 J. J. Liu, S. Y. Lu, Q. L. Tang, K. Zhang, W. X. Yu, H. C. Sun and B. Yang, One-step hydrothermal synthesis of photoluminescent carbon nanodots with selective antibacterial activity against porphyromonas gingivalis, *Nanoscale*, 2017, **9**(21), 7135–7142.
23 D. Kim, G. Jo, Y. Chae, S. Subramani, B. Y. Lee, E. J. Kim, M. K. Ji, U. Sim and H. Hyun, Bioinspired camellia japonica carbon dots with high near-infrared absorbance for efficient photothermal cancer therapy, *Nanoscale*, 2021, **13**(34), 14426–14434.
24 M. P. Shirani, B. Rezaei, A. A. Ensafi and M. Ramezani, Development of an eco-friendly fluorescence nanosensor based on molecularly imprinted polymer on silica-carbon quantum dot for the rapid indoxacarb detection, *Food Chem.*, 2021, **339**, 127920.
25 X. Wang, Y. N. Liu, Q. Z. Wang, T. Bu, X. Y. Sun, P. Jia and L. Wang, Nitrogen, silicon co-doped carbon dots as the fluorescence nanoprobe for trace p-nitrophenol detection based on inner filter effect, *Spectrochim. Acta, Part A*, 2021, **244**, 118876.
26 Y. Zhang, Y. H. He, P. P. Cui, X. T. Feng, L. Chen, Y. Z. Yang and X. G. Liu, Water-soluble, nitrogen-doped fluorescent carbon dots for highly sensitive and selective detection of Hg^{2+} in aqueous solution, *RSC Adv.*, 2015, **5**(50), 40393–40401.
27 F. P. Navarro, M. Berger, S. Guillermet, V. Josserand, L. Guyon, E. Neumann, F. Vinet and I. Texier, Lipid nanoparticle vectorization of indocyanine green improves fluorescence imaging for tumor diagnosis and lymph node resection, *J. Biomed. Nanotechnol.*, 2012, **8**(5), 730–741.
28 S. Sun, L. Zhang, K. Jiang, A. Wu and H. Lin, Toward high-efficient red emissive carbon dots: Facile preparation, unique properties, and applications as multifunctional theranostic agents, *Chem. Mater.*, 2016, **28**(23), 8659–8668.
29 S. J. Zhao, L. Yan, M. Y. Cao, L. Huang, K. Yang, S. L. Wu, M. H. Lan, G. L. Niu and W. J. Zhang, Near-infrared light-triggered lysosome-targetable carbon dots for photothermal therapy of cancer, *ACS Appl. Mater. Interfaces*, 2021, **13**(45), 53610–53617.
30 K. Bilici, S. Cetin, E. Aydindogan, H. Y. Acar and S. Kolemen, Recent advances in cyanine-based phototherapy agents, *Front. Chem.*, 2021, **9**, 707876.
31 J. Li, J. X. Wang, J. Y. Zhang, T. Han, X. Y. Hu, M. M. S. Lee, D. Wang and B. Z. Tang, A facile strategy of boosting photothermal conversion efficiency through state transformation for cancer therapy, *Adv. Mater.*, 2021, **33**(51), 2105999.
32 G. H. Gao, Y. Li and D. S. Lee, Environmental ph-sensitive polymeric micelles for cancer diagnosis and targeted therapy, *J. Controlled Release*, 2013, **169**(3), 180–184.
33 A. Wibrianto, S. Q. Khairunisa, S. C. W. Sakti, Y. L. Ni'mah, B. Purwanto and M. Z. Fahmi, Comparison of the effects of synthesis methods of b, n, s, and p-doped carbon dots with high photoluminescence properties on hela tumor cells, *RSC Adv.*, 2021, **11**(2), 1098–1108.
34 M. Lan, S. Zhao, Z. Zhang, L. Yan, L. Guo, G. Niu, J. Zhang, J. Zhao, H. Zhang, P. Wang, G. Zhu, C.-S. Lee and W. Zhang, Two-photon-excited near-infrared emissive carbon dots as multifunctional agents for fluorescence imaging and photothermal therapy, *Nano Res.*, 2017, **10**(9), 3113–3123.
35 H. Liu, L. Q. Mo, H. L. Chen, C. Chen, J. Y. Wu, Z. L. Tang, Z. Y. Guo, C. F. Hu and Z. M. Liu, Carbon dots with intrinsic bioactivities for photothermal optical coherence tomography, tumor-specific therapy and postoperative wound management, *Adv. Healthcare Mater.*, 2022, **11**(6), 2101448.
36 A. Maleki, J. He, S. Bochani, V. Nosrati, M.-A. Shahbazi and B. Guo, Multifunctional photoactive hydrogels for wound healing acceleration, *ACS Nano*, 2021, **15**(12), 18895–18930.
37 Y. Liang, Y. Liang, H. Zhang and B. Guo, Antibacterial biomaterials for skin wound dressing, *Asian J. Pharm. Sci.*, 2022, **17**(3), 353–384.